



Influence of microalloying on precipitation behavior and notch impact toughness of welded high-strength structural steels

Nina Schroeder¹ · Michael Rhode^{1,2} · Thomas Kannengiesser^{1,2}

Received: 17 May 2024 / Accepted: 7 August 2024
© The Author(s) 2024

Abstract

Microalloying elements such as Nb and Ti are essential to increase the strength of quenched and tempered high-strength low alloy (HSLA) structural steels with nominal yield strength ≥ 690 MPa and their welded joints. Standards such as EN 10025–6 only specify limits or ranges for chemical composition, which leads to variations in specific compositions between steel manufacturers. These standards do not address the mechanical properties of the material, and even small variations in alloy content can significantly affect these properties. This makes it difficult to predict the weldability and integrity of welded joints, with potential problems such as softening or excessive hardening of the heat-affected zone (HAZ). To understand these metallurgical effects, previous studies have investigated different microalloying routes with varying Ti and Nb contents using test alloys. The high-strength quenched and tempered fine-grained structural steel S690QL is the basic grade regarding chemical composition and heat treatment. To evaluate weldability, three-layer welds were made using high-performance MAG welding. HAZ formation was investigated, and critical microstructural areas were identified, focusing on phase transformations during cooling and metallurgical precipitation behavior. Isothermal thermodynamic calculations for different precipitations were also carried out. Mechanical properties, especially Charpy notch impact toughness, were evaluated to understand the influence of different microalloys on the microstructure of the HAZ and mechanical properties.

Keywords High-strength structural steel · Gas metal arc welding · HAZ-softening · Notch impact toughness · Microalloying influences · Thermodynamic simulation

1 Introduction

The use of high-strength low alloy (HSLA) steels has become indispensable in many industrial sectors such as building construction, offshore structures, and mobile crane construction. In that connection, these steels provide economic and ecological potential benefits (e.g., by lightweight construction) due to the combined high strength and toughness [1–3]. Because of increasing service loads

of components, high requirements are placed on the integrity of these steels and their welded joints. For this reason, the chemical composition is of special interest, especially in the addition of microalloying elements such as Nb, Ti, and V, combined with the microstructure adjustment during steel manufacturing [4, 5]. Current standards like EN ISO 10025–6 [6] define the chemical composition of these HSLA steels to achieve the required mechanical properties. Within the standard, steel manufacturers can use a more or less large range for the selection of alloying elements, so that the chemical composition can vary [7]. Considering the weldability of the HSLA steels, their metallurgical behavior in the heat-affected zone (HAZ) is divergent even with the addition of small Nb and Ti amounts in the base metal (BM). Previous investigations on single and three-layer welds with identical filler metal showed that Nb-microalloyed HSLA steel tends to harden in the HAZ [8]. In contrast, Ti-microalloyed steel showed intensive softening in the subcritical and intercritical HAZ regions [8–11]. However, welding fabrication with modern high-performance processes (such as the

Recommended for publication by Commission II - Arc Welding and Filler Metals

✉ Nina Schroeder
nina.schroeder@bam.de

¹ Bundesanstalt Für Materialforschung Und -Prüfung (BAM), Division 9.4–Weld Mechanics, Unter Den Eichen 87, 12205 Berlin, Germany

² Otto-Von-Guericke-University Magdeburg, Institute for Materials Science and Joining Technology, Universitätsplatz 2, 39106 Magdeburg, Germany

modified spray arc) is characterized by high dilution of the BM and the necessary consideration of multiple tempering effects during multi-layer welding. Using different microalloying concepts suggests a divergent mechanical behavior of the welded joint, especially in both the weld metal (WM) and the HAZ.

For example, Jiang et al. and Zhang et al. [12, 13] have discussed the effects of the microstructural characteristics of the base material, HAZ, and WM on fracture toughness. Influences such as grain size [14], hard inclusions [15], M-A (martensite-austenite) phases [16, 17], type of precipitates [18], and their distribution on the cleavage fractures have been analyzed there. For example, Bertolo et al. [19] showed that especially brittle Nb-rich precipitates in a HSLA steel S690QL had the most significant influence on the cracking susceptibility compared to the M-A constituents. The reason was that the Nb-rich inclusions had a higher nano-hardness than the M-A constituents. Other authors [20, 21], however, found no significant effect of precipitates, such as carbides and aluminum oxide precipitates, on the toughness of the intercritical coarse-grained heat-affected zone (ICCGHAZ). Contrasting studies [21, 22] observed that TiN inclusions in bainitic steel could act as crack initiation sites for cleavage fractures in the thermally simulated coarse-grained heat-affected zone (CGHAZ). In [23], the influence of Mo and microalloying elements such as Ti and Nb on precipitation behavior and toughness was investigated. The combination of Mo and Nb showed that the precipitate size and the hardening effect were reduced due to the increase of fine carbides. The higher content of Nb and Mo led to better hardenability and favored the formation of non-polygonal structures such as bainitic ferrite [24]. From the WM perspective, its toughness is highly dependent on the cooling rate and the resulting microstructure, such as acicular ferrite or bainite. Furthermore, dilution between the BM and the filler metal during welding had a major influence on the resulting WM toughness. In that connection, gas metal arc welding (GMAW) with a modified spray arc resulted in a relatively high degree of dilution. It was observed that a Nb-microalloyed S690QL led to a higher Mo content in the

WM because of the increased BM dilution. This favored the bainite formation in combination with high cooling rates, which in turn decreased toughness. However, no significant influence of precipitates on the crack initiation in the WM could be determined within the Charpy test [11].

High-performance multi-layer welding of Ti- or Nb-microalloyed HSLA steels like the S690QL can cause challenges for the mechanical performance of both the WM and HAZ by the combined dilution of the BM and multiple tempering effects by welding of the individual layers. The individual influence on the mechanical properties of dedicated amounts of microalloying elements has hardly been investigated so far. For that reason, in the present study, three-layer welds were carried out for different microalloyed high-strength S690QL using a modified spray arc. Charpy tests were carried out on the respective BM, WM, and HAZ to determine the impact of toughness. In addition, microstructure analyses and fracture surface topography investigations were carried out, and the precipitation behavior was inspected using thermodynamic equilibrium calculations.

2 Materials and methods

2.1 Materials

For a systematic investigation of the influence of microalloying routes on weldability, four melts were produced and heat-treated. The first melt was a conventional S690QL in quenched and tempered (Q + T) condition. Based on this reference grade, two additional alloying routes were investigated. In accordance with HSLA steels in Q + T condition, 15-mm-thick plates were produced by voestalpine Grobblech GmbH, Linz, Austria. Considering the chemical composition limits according to [6], the contents of Ti and Nb were systematically varied. The chemical composition in accordance with the standard is shown in Table 1 (BM: Stand.). The values specified in the standard represent the maximum limit values for the chemical composition. The reference melt of S690QL did not contain any Ti or Nb. Grade “A”

Table 1 Chemical composition in wt.% of tested materials by OES (Fe-balance)

Element	C	Si	Mn	Cr	Cu	Mo	Ni	Al	Nb	Ti	N	CET ^b	CEV ^b
BM: Stand. ^a	0.20	0.80	1.70	1.50	0.50	0.70	4.0		0.06	0.05	0.015		0.65
BM: Ref	0.09	0.30	1.61	0.18	0.02	0.30	0.19	0.10	-	-	0.0063	0.30	0.47
BM: A (Nb)	0.07	0.29	1.54	0.17	0.02	0.29	0.18	0.10	0.025	-	0.0059	0.27	0.43
BM: B (Ti)	0.07	0.30	1.53	0.17	0.02	0.30	0.19	0.10	-	0.015	0.0055	0.27	0.44
WM: G69 ^c	0.09	0.43	1.32	0.2	0.09	0.55	1.43	0.002	0.001	0.019	0.007	0.33	0.56

^aEN 10025-6 S690QL

^bEN 1011-2

^cEN ISO 16834-A-G 69 6 M Mn4Ni1.5CrMo, chemical composition in accordance with the manufacturer's test report

represented Nb-alloyed steel and grade “B” Ti-microalloyed steel. For the welding experiments, a solid filler wire (\varnothing 1.2 mm) was used. The strength class corresponds to a commercial G69 filler wire (according to ISO 16834 [25]). The calculated carbon equivalents (CET and CEV) [26, 27] are shown for comparison. The calculated carbon equivalent suggests that the weldability is generally good, and the susceptibility to cold cracking is low. The chemical composition was identified by optical emission spectroscopy (OES) using a SPECTROTEST system (SPECTRO Analytical Instruments GmbH, Germany) (Table 1). Table 2 shows the mechanical-technological properties of the tested materials.

2.2 Welding experiments

Three-layer welds under free shrinkage conditions were produced using automated metal active gas (MAG) welding, and an alpha Q 552 welding source (EWM GmbH, Germany) was used for the welds. The characteristic power range (controlled by the U/I parameter) of the modified spray arc was applied. Thus, a V-groove welding plate preparation

with a total opening angle of 30° was realized (i.e., machining of 15° angle for each welding plate), see Fig. 1c. The total length of the weld seam was 300 mm, and the width per weld plate was 150 mm. The preheating and interpass temperature were maintained at 100°C . The shielding gas was M21 (in accordance with DIN EN ISO 14175 [28]) with 82% Ar and 18% CO_2 . The welding speed was kept constant at 400 mm/min. The DC polarity was used with a welding current from 262 to 280 A and arc voltage from 24 to 26 V. The average welding heat input was 1 kJ/mm, and the average $\Delta t_{8/5}$ time (measured by laser pyrometer) was 7.8 s. To observe the cooling conditions during and after welding, four types of K thermocouples (thermos-wire thickness of 0.25 mm) were applied on the top and root side of the welding sample as shown in Fig. 1a and c.

2.3 Metallographic analyses and hardness tests

The samples for the metallographic investigations were cut from the welded plates transverse to the welding direction and from the center of the weld seam. They were embedded

Table 2 Mechanical properties of the tested materials

Property	Yield strength, $R_{p0.2}$ (MPa)	Tensile strength, R_m (MPa)	Elongation at fracture, A_5 (%)	Impact toughness, $A_v: -40^\circ\text{C}$ (J)	Hardness (HV)
BM ^s ^a	690	770 to 940	14	Min. 27	284.2 (HV1) ^c
WM: G 69 ^b	733	811	21.4	87.7 (64 J at -60°C)	264.3 (HV10)

^aEN 10025-6 S690QL, properties in accordance with the standard

^bEN ISO 16834-A-G 69 6 M Mn4Ni1.5CrMo, properties from the producer’s test report

^cHardness testing

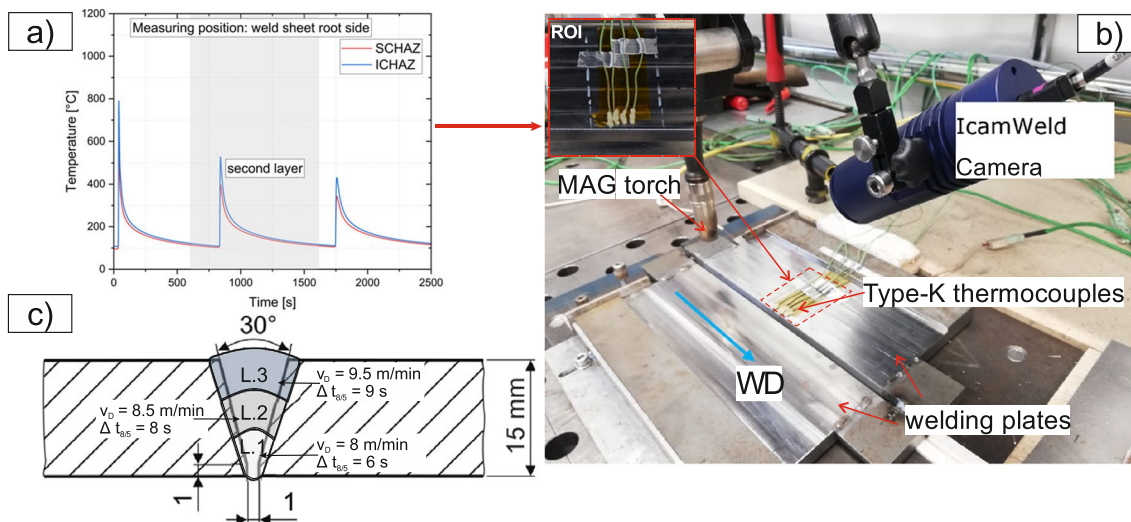


Fig. 1 Welding experiment: **a** exemplary T-t curves from the ICHAZ and SCHAZ area, measured on the weld root side; **b** test set-up for welding tests (WD=welding direction) with positions of type-K ther-

mocouples, top side (arrangement root side mirrored); and **c** illustration of seam layer set-up of a three-layer weld

in an electrically conductive embedding compound, mechanically ground, and polished to 1 μm . Finally, they were etched with 2 wt.% Nital etchant for 10 to 15 s at room temperature. In addition, HV1 hardness measurement rows (according to ISO 6507–1) were located along each layer to allow a quantitative statement about the hardness distribution. The distance between each hardness indentation in both the WM and BM was 0.50 mm, and the distance in the HAZ was 0.25 mm.

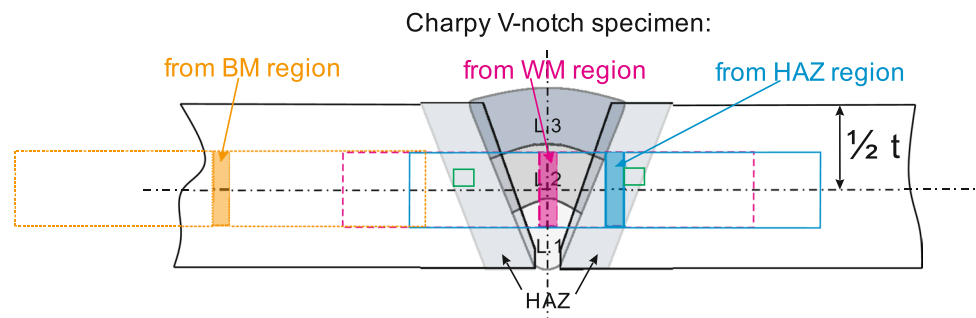
The fracture surfaces of Charpy V-notch specimen areas were evaluated using the ImageJ (version: 1.52e, developed by Wayne Rasband from the National Institutes of Health, USA) image processing software. Macro photographs of the fracture surfaces were previously taken using a Canon EOS 600D SLR camera. The microprobe analysis to determine the Mo distribution in the HAZ was carried out with a JEOL microprobe JXA-8900 RL. The mapping to visualize the element distribution was carried out with 15 kV acceleration voltage, 100 ms counting time, and 75 nA probe current. The map size was approx. 250 μm^2 (number of increments 250 \times 250 μm^2 , incremental steps of 1 μm).

2.4 Charpy V-notch impact toughness test

For each material shown in Table 1, three specimens were machined from both the WM and HAZ regions (with the prior etching of the HAZ samples described in Section 2.3 to identify a sufficient notch position). Charpy V-notch specimens were also machined from the BM for comparison purposes. To ensure an identical thermal cycle history of the samples, they were machined from the mid-plate thickness region with the dimensions of 55 mm width \times 10 mm thickness \times 10 mm length, as shown in Fig. 2. The Charpy impact tests were carried out at $-40\text{ }^\circ\text{C}$ according to EN ISO 148–1:2017 [29]. For that purpose, a pendulum impact tester of the model HIT750P (Zwick Roell GmbH, Germany) was used.

The appearing fracture surface topography after the impact testing was analyzed using a scanning electron microscope (SEM) Phenom XL (from Thermo Fisher) at an acceleration voltage of 15 kV using a secondary electron detector (SED).

Fig. 2 Schematic illustration of V-notched impact specimens extraction locations from the welded plate (colored areas represent the V-notch respectively the location of the notch of the Charpy specimen)



2.5 Thermodynamic simulation of precipitation kinetics

Complementary to the experimental investigations, thermodynamic modeling was carried out using the Thermo-Calc 2022b software (for thermodynamic equilibrium phase diagrams) [30] and the application of the TC-PRISMA module (simulation of precipitation behavior). In the present work, the Fe-database “TCFE11” and the kinetics database “MOBFE6” were used. To determine the precipitation behavior of the three differently microalloyed base materials, phase diagrams were calculated in the equilibrium state (all alloying elements from Table 1). Their volume fraction (based on a total system size = 1 mol) was calculated as a function of temperature (range between 500 and 1600 $^\circ\text{C}$). This provided fundamental insights into the differences between the materials regarding their precipitation behavior in the equilibrium state.

3 Results and discussion

3.1 Base metal characterization

In this section, the metallurgical behavior of the three investigated base materials before welding is analyzed and presented in detail.

3.1.1 Precipitation behavior in an equilibrium condition

Basic phase diagrams of the different microalloyed grades were calculated using Thermo-Calc. This allowed the prediction of both the type and respective temperature range of the occurring precipitates. Figure 3 shows the volume fractions of precipitates that precipitate in the austenite phase region as a function of the temperature of all three investigated BMs in the equilibrium state. The S690 QL reference sample, without Ti and Nb, only shows precipitates in terms of aluminum nitrides at 1191 $^\circ\text{C}$, the phase volume fraction settles at 4.4×10^{-4} mol when cooled to 500 $^\circ\text{C}$. Aluminum serves both as a deoxidization element during steelmaking and as a grain refiner [31]. The steel grades

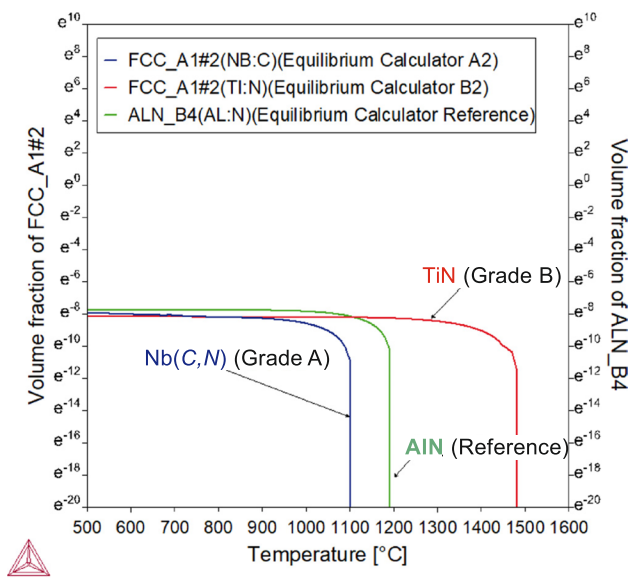


Fig. 3 Equilibrium phase fraction of precipitates for each investigated BM (in as-received condition)

A and B contained the same amount of Al as the reference grade (deoxidation element for the melt). The precipitation behavior of grade A (Nb-alloyed) shows Nb-bearing

carbonitrides at 1100 °C. The final phase fraction after cooling is 3.6×10^{-4} mol. Grade B (Ti-alloyed) only shows TiN precipitates at 1478 °C in equilibrium condition, with a phase fraction of 2.9×10^{-4} mol.

It must be noted that the conducted simulations represented the “ideal” thermodynamic equilibrium condition and must be viewed with caution, as welding represents a non-equilibrium due to its welding thermal temperature cycles with rapid heating, short holding times, and rapid cooling. Nevertheless, these simulations could provide initial indications of the precipitation behavior.

3.1.2 Microstructure of base materials

Figure 4 shows the SEM images of the three BMs and a respective image of the WM (from the first filler layer, once tempered by the final cover layer, both at a magnification of 4200). All three BMs show a typical HSLA-steel complex microstructure (Fig. 4a–c). This encompasses martensite (M), auto-tempered martensite (ATM), and coalesced martensite (CM). The microstructure of the WM (Fig. 4d) consists of acicular ferrite (AF). The Vickers hardness of the three base materials investigated was analyzed to be between 281 and 331 HV1, and the hardness in the WM of the second

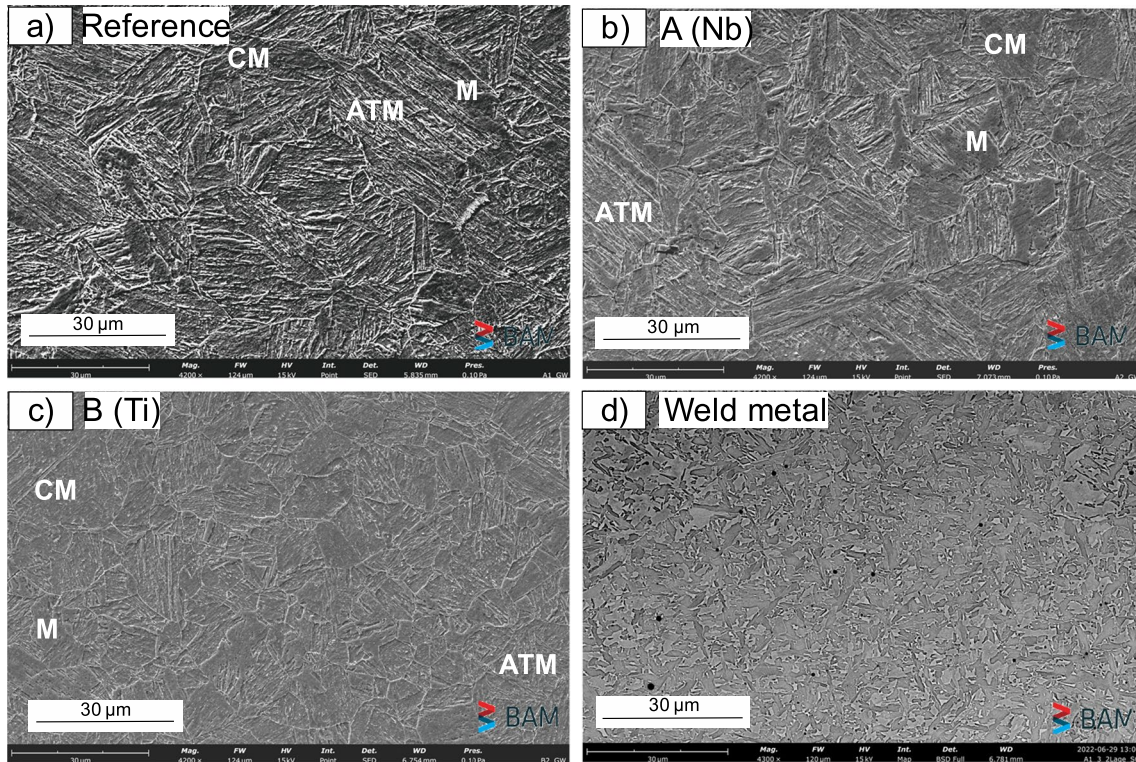


Fig. 4 SEM figure of BMs and WM: **a** S690QL reference without Nb and Ti, **b** WM microstructure, **c** BM grade A (with Nb), and **d** BM grade B (with Ti)

layer was between 245 and 287 HV1. The grain size of the three steel grades is between 12.2 and 15.7 μm [9].

3.2 Charpy V-notch toughness

3.2.1 Base materials

The investigation of the impact toughness showed a clear difference (Fig. 5a). The reference alloy had an impact toughness of 101.7 ± 47.4 J, whereby the SEM evaluation of the fracture surface areas showed a predominantly ductile fibrous zone (F) of 40% of the total fracture surface area, see Fig. 5b. This was characterized by a ductile fracture surface topography with small dimples (Fig. 6a). Microalloying route A (Nb), which contained only Nb as a microalloying element, exhibited a mixed fracture behavior, with a predominance of cleavage fracture radial zone (R) with 81%. The impact toughness was 55.6 ± 17.8 J. Both the reference alloy and grade

A (Nb-alloyed) achieved the required minimum impact energy of $KV_2 = 27$ J at -40 °C for transverse specimens, in accordance with [6]. Grade B (Ti-alloyed) showed a very high proportion of cleavage fracture (86%, see Figs. 5b and 6c) and an impact toughness of 36.1 ± 25.8 J, which must be evaluated critically with regard to the relatively high standard deviation. In addition, grade B (Ti-alloyed) showed large inclusions on the fracture surface. It was shown in [32] that coarse Ti inclusions, which are irregularly distributed in the matrix, can serve as potential cleavage fracture incubators for the formation of microcracks. This can explain severe deviations in the impact toughness values. Inclusion in sample B (Ti-alloyed) could be identified as a multi-element inclusion (see EDX spot analysis in Fig. 6c). Due to the identified composition and considering the thermal stability (see Fig. 3), an aluminum oxide formed first, followed by titanium nitrides alongside with manganese sulfides [33]. However, these inclusions were not identified here as crack initiation sites, as no

Fig. 5 Charpy impact test results of BMs: **a** impact energy, **b** exemplary macrograph of fracture surface of a V-notched impact specimen with percentage share of fibrous (F) zone, (S) shear lip zone, and (R) radial zone in [%]

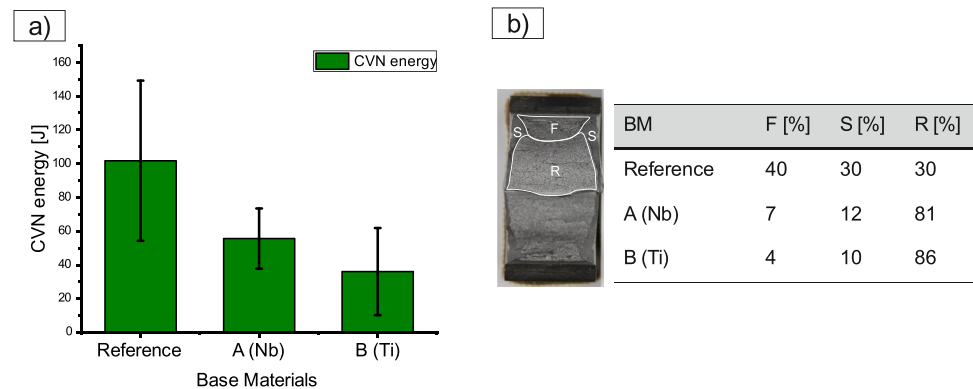
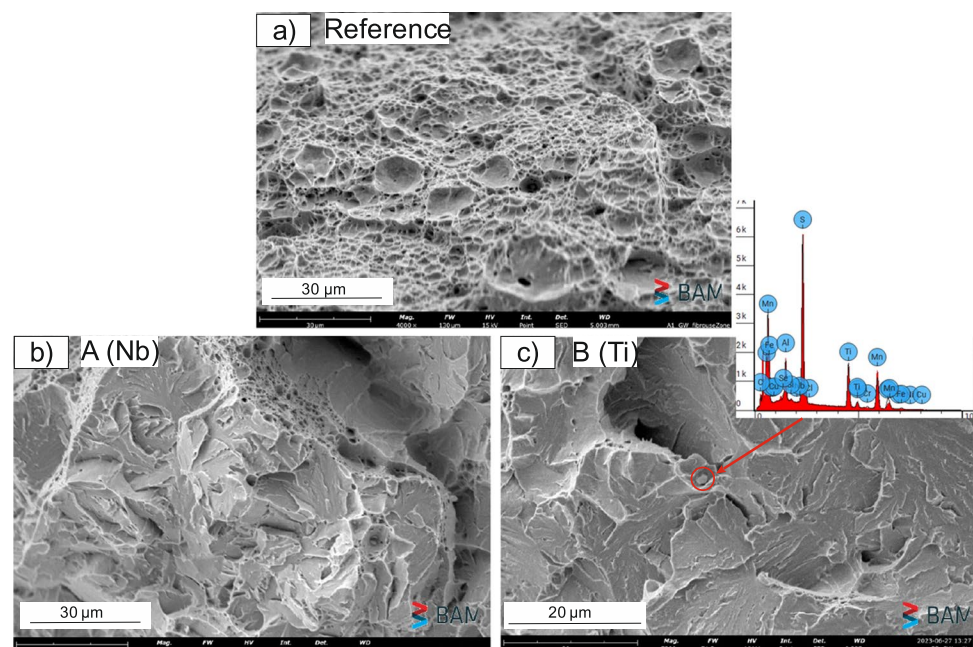


Fig. 6 Exemplary fracture surface topographies of the investigated BMs. The images shown represent the highest proportion of the measured surface topography according to Fig. 5b: **a** reference, **b** grade A (Nb-alloyed), and **c** grade B (Ti-alloyed)



typical crack propagation across the interfaces between particle (TiN inclusion) and matrix was recognized here.

3.2.2 Heat-affected zone

To justify the impact toughness behavior of the HAZ of the welded BMs, the metallurgical behavior in the specific HAZ must be understood in depth. HSLA steels are known to exhibit softening in the HAZ during welding, i.e., a significant reduction in hardness in the HAZ compared to the WM and the BM [8, 34]. Vickers hardness series was set to analyze the hardness distribution in the individual layers. Based on the symmetry of the weld seam and the resulting symmetrical thermal conduction, aligned hardness measuring spots were set from the center of the weld seam. The hardness distribution in the top and filler layers along the WM via the HAZ to the BM of the three welded BMs showed

the following results (Fig. 7). Thus, the strong influence of the tempering effect in the HAZ can be recognized in the filling layer.

On the one hand, hardening effects can be seen in the top layer due to the lack of further tempering in the subsequent layers, and on the other hand, the “hardening sink” can be seen between the hardening area and the BM. Due to the 30 V seam preparation, the filler layer has a narrower WM and HAZ area than the top layer. Due to the intense tempering effects caused by the final top layer, the material is recrystallized, resulting in a reduction of the hardness in the HAZ of the intermediate filler layer (240 HV1 compared to 350 HV1 of the top layer). For that reason, the notched impact samples were taken from the mid-plate thickness region (1/2 * thickness), i.e., where the first filler layer is mainly located). Figure 8 shows additional light optical microscope (LOM) micrographs of the tempering areas of

Fig. 7 Hardness distribution in the top and filler layer of all three welded BMs

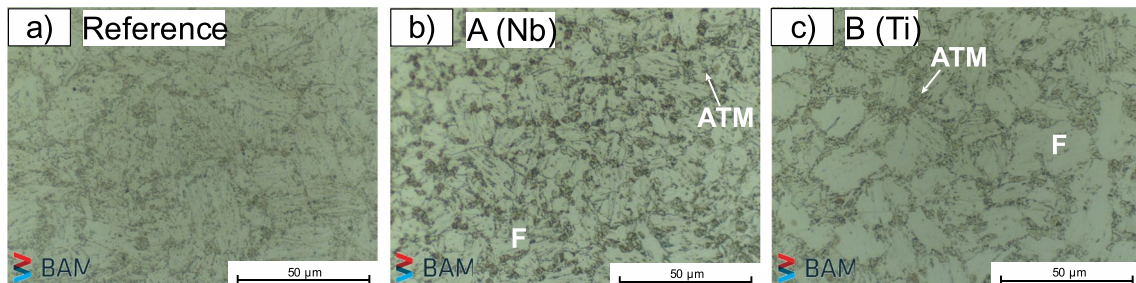
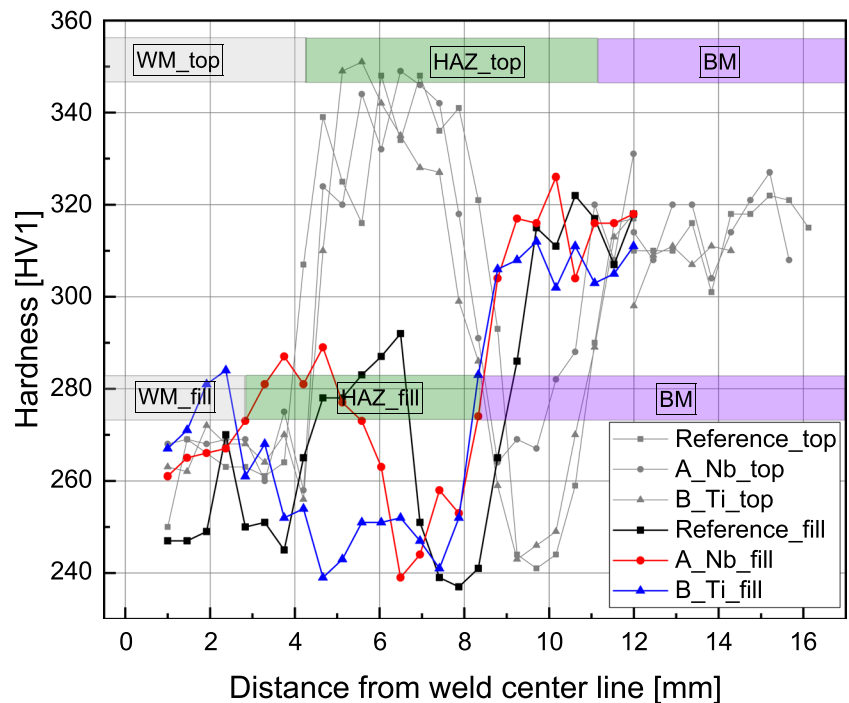


Fig. 8 LOM micrographs of tempered HAZ investigated BMs, i.e., regions of the lowest hardness: **a** reference grade, **b** grade A (Nb-alloyed), and **c** grade B (Ti-alloyed)

the filler layers of the three welded BMs (see areas marked in green in Fig. 2). These additional LOM micrographs were taken because of the better contrast range of the optical microscope images compared to the SEM. The investigated area was exposed to temperatures between 700 and 500 °C due to the multi-layer welding (see Fig. 1a). Evaluating the micrographs, a divergent phase distribution between the three BMs was recognized. The most significant difference was identified between grade A (Nb-microalloyed) and grade B (Ti-microalloyed). The Nb-microalloying results in a significantly increased share of ATM and a limited amount of ferrite. Furthermore, it can be assumed that carbide clusters form within ATM at these temperatures [16, 35]. Previous studies have shown that a high amount of carbide-forming elements such as Mo and/or Cr increases the resistance to softening by reducing the driving force of the tempering reaction, e.g., by stabilizing the martensite [36–38]. Therefore, electron probe-microanalyses EMPA in the HAZ (see Fig. 9a–c) have shown that, in contrast to the reference and grade B (Ti-microalloyed), Mo accumulates in the outer HAZ of grade A (Nb-microalloyed) (see Fig. 9b).

In addition, Mo is known to form secondary carbides at lower temperatures during tempering. The tempering reaction can thus be retarded. As a result, grade A (Nb-microalloyed) was more tempering resistant. A considerable

secondary hardening effect in the HAZ was not observed, as this phenomenon can typically only be observed with longer holding times > 500 °C [38, 39]. In contrast to grade A, this kind of delayed tempering was not observed in grade B (Ti-microalloyed). The microstructure consists of a necklace-like arrangement of ATM along the prior austenite grain boundaries (PAGBs) and a high volume fraction of ferrite (see Fig. 8c). In contrast to grade A (Nb-microalloyed), Mo was homogeneously distributed in the HAZ and did not form clusters (see Fig. 9c). It was reasonable to assume that Nb and Mo had a combined, synergistic effect. Further studies showed that the addition of Nb and Mo decelerates static recrystallization [37, 40, 41].

The S690QL reference (without Ti or Nb) did not show a pronounced tempering resistance. In that case, the ATM appeared to be “blurred” or decomposed into ferrite (see Fig. 8a). This indicates that microalloying by Nb and Ti has a major influence on the tempering resistance.

As shown in Fig. 10a, the impact toughness of the HAZ showed that all tested HAZ specimens reached the required standard specifications of > 27 J at a test temperature of –40 °C. The HAZ of the reference grade had an impact toughness of 75.5 ± 31.7 J, the HAZ of grade A (Nb-microalloyed) showed 79 ± 39 J, and the HAZ of grade B (Ti-microalloyed) had the highest toughness of

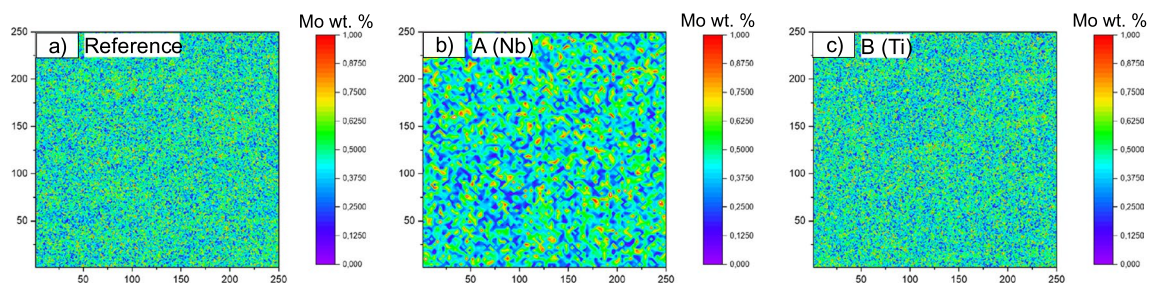
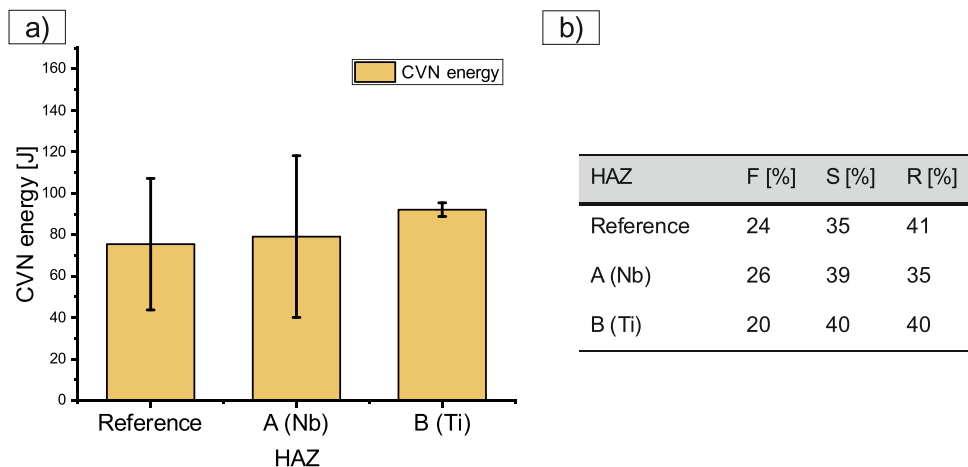


Fig. 9 Corresponding EMPA mapping of Mo distribution in HAZ: **a** reference grade, **b** grade A (Nb-alloyed), and **c** grade B (Ti-alloyed)

Fig. 10 a Impact energy of investigated HAZ and **b** fracture topography fraction of investigated HAZ



92 ± 3.3 J (i.e., > 2.6 times of the corresponding BM). This could be explained by the different microstructures in the tempered HAZ (compared to Fig. 8) and the resulting softening in all investigated alloys (compared to Fig. 7). The corresponding percentage fraction of the fibrous (F), shear (S), and cleavage fracture radial zone (R) is shown in Fig. 10b. The corresponding fracture surface topography can be found in Fig. 11a–c.

The fracture surface topographies exemplarily shown in Fig. 11a–c were taken from the R-area of the HAZ impact samples and recorded via SEM (magnification $\times 4000$). All fracture topographies indicate a transgranular quasi-cleavage fracture with a small fraction of ductile fracture (characterized by isolated dimpled regions). Significant differences in the fracture surface topography of the three HAZ could not be identified.

A determination of the toughness properties of the HAZ based on selected specimens must be viewed critically, as the results of the notched impact toughness are not only dependent on the position and location of the machined notch, but also on the weld geometry and shape. Furthermore, the results of the Charpy impact tests of the HAZ must be viewed with caution here, as only two impact samples were available per alloy due to material limitations.

3.2.3 Weld metal

Figure 12a shows the Charpy impact test results of the WM, and Fig. 12b shows the percentage share of the respective F-, S-, and R-zone. It should be noted that both the chemical composition of the G69 filler wire and the welding conditions (heat input) were identical for all welding experiments, i.e., similar cooling conditions were applied. Differences in the final chemical composition and microstructure of the WM are mainly attributed to the Nb or Ti alloy element pick-up by the dilution of the different BMs. The WM microstructure consisted mainly of AF with round precipitates and complex Al, Ti, and Mn inclusions (with several μm in size). This was also reported in reference [9]. The minimum WM hardness of the S690QL reference grade was 247 HV1, for grade A (Nb-microalloyed) 261 HV1, and for grade B (Ti-microalloyed) 252 HV1 (see Fig. 7).

The impact absorbed energy values of the WM specimens varied moderately. This could be attributed to the heterogenous WM microstructure or to welding imperfections such as for example micropores. Nevertheless, the CVN energy values were comparable to the HAZ samples but met the requirements of > 47 J at -40 °C, in accordance with [25]. The WM of the S690QL reference grade had an impact toughness of 66.6 ± 27.5 J compared to grade A

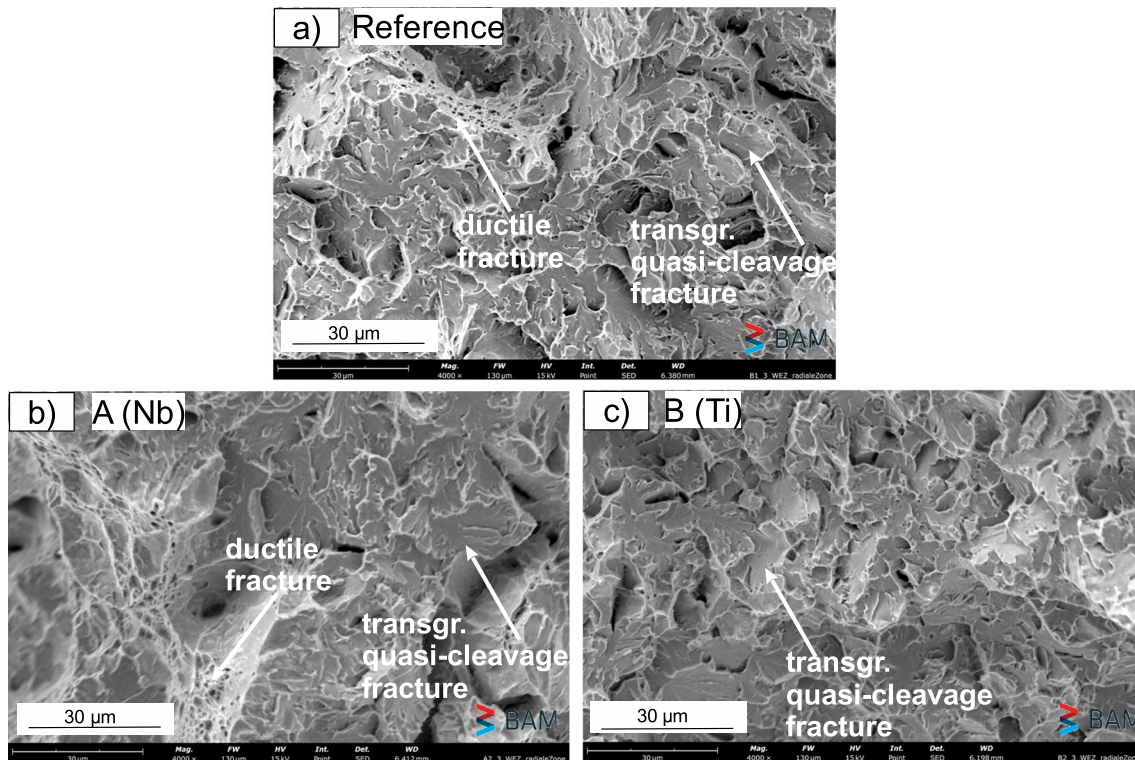
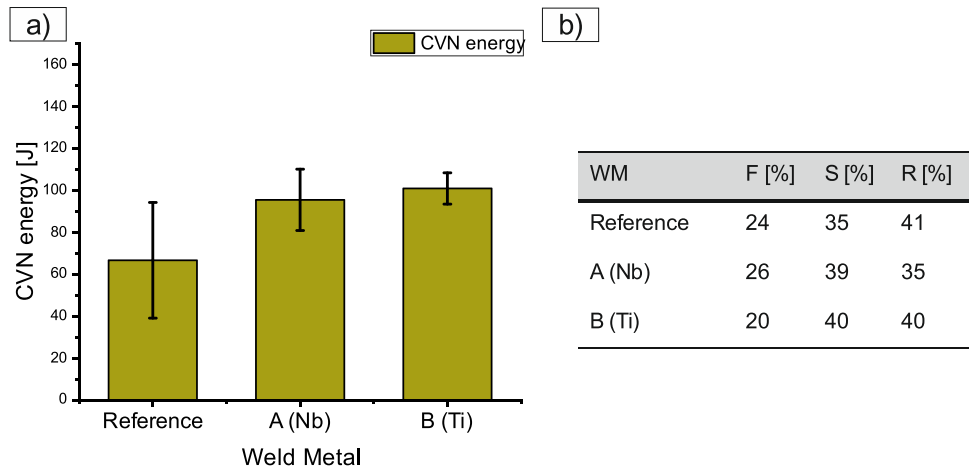


Fig. 11 Exemplary fracture surface topography of investigated Charpy samples for all three HAZ microstructures: **a** S690QL reference grade, **b** grade A (Nb-alloyed), and **c** grade B (Ti-alloyed)

Fig. 12 **a** Impact energy of investigated WM and **b** fracture surface fractions of three investigated HAZ



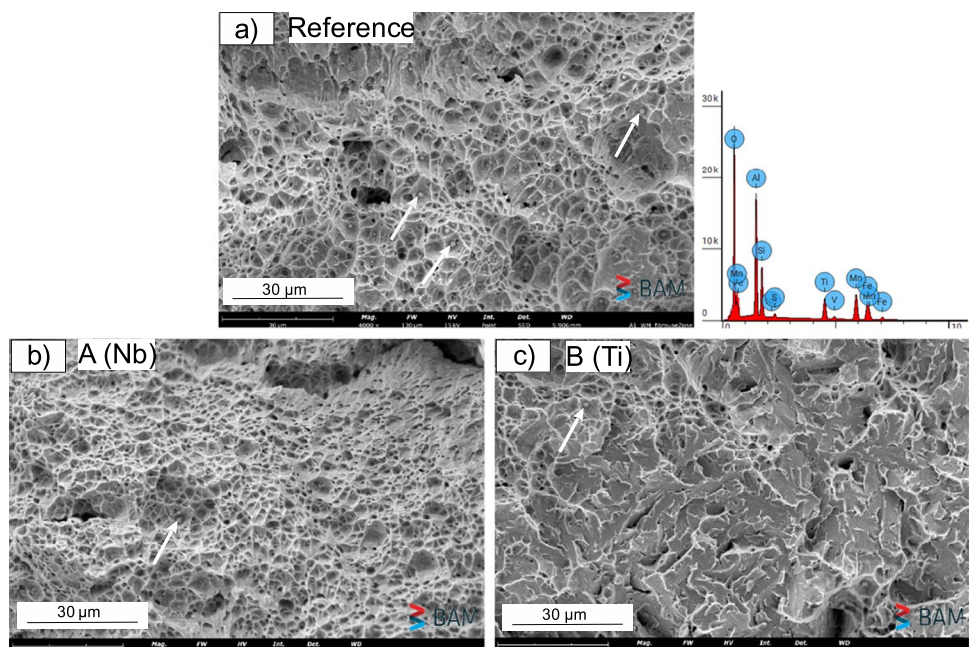
(Nb-microalloyed) with 95.4 ± 14.6 J. Grade B (Ti-microalloyed) had the highest impact toughness of 100.8 ± 7.5 J. According to [25], only one value of the impact energy out of three samples can be < 47 J but must be a minimum of 32 J. This was the case for the reference grade with 35.11 J for one sample.

These relatively high impact energies of all investigated WM samples can be explained by the predominant AF microstructure, which is characterized by its high toughness [42] compared to bainite. In addition, the dilution of the BM and the intermixing with the welding wire composition play a major role. In that connection, the degree of BM dilution is characterized by the initial weld seam geometry vs. the final weld seam (fusion line) and determined via cross-sections [10], i.e., which share of the BM is melted during welding. Considering this, the average dilution in

all three welded alloys was 41%. This means that a high portion of the respective BM alloying elements was present in the final solidified WM. Hence, the different intermixed WM compositions had a significant influence on the impact toughness. For example, it is well known that titanium and its precipitates are excellent nucleation promoters for the occurrence of AF with the mentioned high toughness [11, 43]. This could be proven for both the WM of grades A and B compared to the reference BM. From that point of view, a careful selection of microalloying elements is suggested.

Figure 12b shows the evaluation of the percentage share of the F-, S-, and R-zone. The corresponding fracture topographies can be found in Fig. 13a–c. The analysis was carried out on samples that had no imperfections such as porosities in the WM. The reference material and grade A (Nb-microalloyed) showed a high proportion of shear lip zone

Fig. 13 Exemplary fracture surface topography of intermixed WM of G69 filler wire welded to **a** reference grade, **b** grade A (Nb-microalloyed), and **c** grade B (Ti-microalloyed)



($S_{\text{Reference}}$: 43% and $S_{\text{A(Nb)}}$: 69%, Fig. 12b). Figure 13a and b shows fracture surfaces from the shear lip zone of investigated alloys. These fracture surfaces indicate a ductile behavior due to finely distributed cavities/dimples, which are characteristic of high toughness. Within the dimples that formed during plastic deformation, there were round inclusions (Fig. 13a–c, marked with a white arrow for the investigated materials). The inclusions were identified as Al- or Si-oxides (using EDX spot analysis). The WM of grade B (Ti-microalloyed) showed a high proportion of quasi-cleavage fractures (with $R=68\%$, as shown in Fig. 13c), i.e., a pronounced brittle fracture. The quasi-cleavage fracture surfaces or cleavage planes were connected by tear ridges and shallow dimples. Small inclusions within dimples and cleavage facets were identified and could be also characterized as Al- or Si-oxides.

4 Conclusions

In this study, the metallurgical influence of various microalloyed HSLA steel of strength class S690QL on the impact toughness was analyzed. In particular, the influence of Nb and Ti as microalloying elements in the BM was analyzed separately. For this purpose, three-layer welds were carried out, and notched bar samples for the Charpy impact test were extracted to analyze the impact toughness at $-40\text{ }^{\circ}\text{C}$ in WM, HAZ, and BM. The following conclusions can be drawn from the results presented:

- The tempering resistance of the HSLA S690QL was highly dependent on the microalloying elements. For example, grade A (Nb-microalloyed) was reported to have a higher tempering resistance in both the intercritical HAZ and subcritical HAZ. This was explained by the synergetic interplay of Mo and Nb, which retards the martensite decay in the tempering regions and thus prevented the steel from softening significantly in the HAZ during welding.
- The BM of grade B (Ti-microalloyed) partially failed to meet the standard requirement of 27 J at $-40\text{ }^{\circ}\text{C}$ in the Charpy test. This was supported by the findings of the mostly cleavage-like fracture topography. From this point of view, the impact toughness of Ti-microalloyed S690QL must be carefully evaluated.
- The HAZ of grade B (Ti-microalloyed) showed a high impact toughness (almost 3 times that of the BM) because the hardened microstructure consisted of large ferrite plates and a necklace structure of ATM along the PAGBs. The crack propagated as a transgranular quasi-cleavage fracture.
- The good impact toughness properties of all WM samples can be explained by the high degree of dilution between

the base and deposited WM, with AF as the predominant microstructure regardless of the chemical composition.

Acknowledgements The authors would like to thank voestalpine Grob-blech GmbH (Linz, Austria) for providing the test materials. We would like to thank Peter Friedersdorf and Thomas Michael for their support during the welding tests. We thank Marina Marten for the metallographic sample preparation and hardness measurements. For the EPMA investigation, Gabriele Oder is thanked as well as Peter Wossidlo for the assistance in conducting the Charpy tests (all with Bundesanstalt für Materialforschung und -prüfung, Berlin, Germany).

Funding Open Access funding enabled and organized by Projekt DEAL. The current study was a part of the research project “Investigation of the softening mechanism during welding in the heat-affected zone of microalloyed high-strength steels” funded by the German Research Foundation DFG, research grant no. 435083436. Open access funding by Projekt DEAL is gratefully acknowledged.

Data availability The raw data is not accessible by the public but can be shared on demand with private access.

Declarations

Competing interests The authors declare no competing interests.

Open Access This article is licensed under a Creative Commons Attribution 4.0 International License, which permits use, sharing, adaptation, distribution and reproduction in any medium or format, as long as you give appropriate credit to the original author(s) and the source, provide a link to the Creative Commons licence, and indicate if changes were made. The images or other third party material in this article are included in the article’s Creative Commons licence, unless indicated otherwise in a credit line to the material. If material is not included in the article’s Creative Commons licence and your intended use is not permitted by statutory regulation or exceeds the permitted use, you will need to obtain permission directly from the copyright holder. To view a copy of this licence, visit <http://creativecommons.org/licenses/by/4.0/>.

References

1. Caballero FG, Santofimia MJ, García-Mateo C, Chao J, de Andrés CG (2009) Theoretical design and advanced microstructure in super high strength steels. *Mater Des* 30(6):2077–2083. <https://doi.org/10.1016/j.matdes.2008.08.042>
2. Villalobos JC, Del-Pozo A, Campillo B, Mayen J, Serna SM, steels through history until, (2018) review of chemical composition, processing and hydrogen service. *Met* 2018:8. <https://doi.org/10.3390/met8050351>
3. Xie H, Du L-X, Hu J, Misra RDK (2014) Microstructure and mechanical properties of a novel 1000MPa grade TMCP low carbon microalloyed steel with combination of high strength and excellent toughness. *Mater Sci Eng A* 612:123–130. <https://doi.org/10.1016/j.msea.2014.06.033>
4. Gladman T (1999) Precipitation hardening in metals. *Mater Sci Technol* 15(1):30–36. <https://doi.org/10.1179/026708399773002782>
5. Mohrbacher H (2011) Mo and Nb alloying in plate steels for high-performance applications. *International Symposium on the Recent Development in Plate Steels*. pp 169–178

6. DIN EN 10025–6:2019+A1:2022, in Hot rolled products of structural steels – Part 6: Technical delivery conditions for flat products of high yield strength structural steels in the quenched and tempered condition. 2023, Beuth Verlag GmbH: Berlin
7. Dainelli P, Maltrud F (2012) Management of welding operations with high strength steels. *Soud et Tech Connex* 66(7–8):33–38
8. Zhang L, Kannengiesser T (2016) HAZ softening in Nb-, Ti- and Ti plus V-bearing quenched and tempered steel welds. *Weld World* 60(2):177–184. <https://doi.org/10.1007/s40194-016-0299-7>
9. Schroeder N, Rhode M, Kannengiesser T (2023) Thermodynamic prediction of precipitations behaviour in HAZ of a gas metal arc welded S690QL with varying Ti and Nb content. *Weld World* 67(9):2143–2152. <https://doi.org/10.1007/s40194-023-01550-2>
10. Zhang L Microstructure-property relationship in microalloyed high-strength steel welds, ed. B.D. (155). 2017, Berlin: Eigenverlag Bundesanstalt für Materialforschung und-prüfung (BAM)
11. Zhang L, Pittner A, Michael T, Rhode M, Kannengiesser T (2015) Effect of cooling rate on microstructure and properties of microalloyed HSLA steel weld metals. *Sci Technol Weld Join* 20(5):371–377. <https://doi.org/10.1179/1362171815y.000000026>
12. Jiang Q, Bertolo VM, Pallaspuro S, Popovich V, Sietsma J, Walters CL (2023) Microstructure-based cleavage parameters in bainitic, martensitic, and ferritic steels. *Eng Fract Mech* 281:109146. <https://doi.org/10.1016/j.engfracmech.2023.109146>
13. Zhang T, Yu H, Li Z, Kou S, Kim HJ, Tillmann W (2021) Progress on effects of alloying elements on bainite formation and strength and toughness of high strength steel weld metal. *Mater Res Express* 8(3):032002. <https://doi.org/10.1088/2053-1591/abea58>
14. Miyata T, Yang R, Otsuka A, Haze T, Aihara S (1989) Cleavage fracture of steels with fine grained ferrite, coarse grained bainitic and martensitic microstructures. *ICF7 Adv in Fract Res* 4:2563–2572
15. Ray A, Paul SK, Jha S (1995) Effect of inclusions and microstructural characteristics on the mechanical properties and fracture behavior of a high- strength low- alloy steel. *J Mater Eng Perform* 4(6):679–688. <https://doi.org/10.1007/BF02646444>
16. Bertolo V, Jiang Q, Terol Sanchez M, Riemslog T, Walters CL, Sietsma J, Popovich V (2023) Cleavage fracture micromechanisms in simulated heat affected zones of S690 high strength steels. *Mater Sci Eng A* 868:144762. <https://doi.org/10.1016/j.msea.2023.144762>
17. Li X, Ma X, Subramanian SV, Shang C, Misra RDK (2014) Influence of prior austenite grain size on martensite–austenite constituent and toughness in the heat affected zone of 700MPa high strength linepipe steel. *Mater Sci Eng A* 616:141–147. <https://doi.org/10.1016/j.msea.2014.07.100>
18. Zhou M-W, Yu H (2012) Effects of precipitates and inclusions on the fracture toughness of hot rolling X70 pipeline steel plates. *Int J Miner Metal Mater* 19(9):805–811. <https://doi.org/10.1007/s12613-012-0632-0>
19. Bertolo V, Jiang Q, Scholl S, Petrov RH, Hangen U, Walters C, Sietsma J, Popovich V (2022) A comprehensive quantitative characterisation of the multiphase microstructure of a thick-section high strength steel. *J Mater Sci* 57(13):7101–7126. <https://doi.org/10.1007/s10853-022-07121-y>
20. Li Y, Baker TN (2010) Effect of morphology of martensite–austenite phase on fracture of weld heat affected zone in vanadium and niobium microalloyed steels. *Mater Sci Technol* 26(9):1029–1040. <https://doi.org/10.1179/026708309X12512744154360>
21. Vassilaros MG (1990) Fracture behavior of ultra-low-carbon steel plate and heat-affected-zone, DTIC report, ADA235638
22. Echeverría A, Rodriguez-Ibabe JM (2003) The role of grain size in brittle particle induced fracture of steels. *Mater Sci Eng A* 346(1):149–158. [https://doi.org/10.1016/S0921-5093\(02\)00538-5](https://doi.org/10.1016/S0921-5093(02)00538-5)
23. Larzabal G, Isasti N, Rodriguez-Ibabe JM, Uranga P (2017) Evaluating strengthening and impact toughness mechanisms for ferritic and bainitic microstructures in Nb, Nb-Mo and Ti-Mo microalloyed steels. *Met* 7. <https://doi.org/10.3390/met7020065>
24. Isasti N, Jorge-Badiola D, Taheri ML, Uranga P (2013) Phase transformation study in Nb-Mo microalloyed steels using dilatometry and EBSD quantification. *Metall Mater Trans A* 44(8):3552–3563. <https://doi.org/10.1007/s11661-013-1738-3>
25. DIN EN ISO 16834, in Welding consumables – wire electrodes, wires, rods and deposits for gas shielded arc welding of high strength steels – classification (ISO 16834:2012). 2012, Beuth Verlag GmbH: Berlin
26. EN 1011–2, in Welding-recommendations for welding of metallic materials-Part 2: Arc welding of ferritic steels. 2001, Beuth Verlag GmbH: Berlin
27. Dearden J (1940) A guide to the selection and welding of low alloy structural steels. *Inst Weld Trans* 3:203
28. DIN EN ISO 14175, in Welding consumables – gases and gas mixtures for fusion welding and allied processes (ISO 14175:2008). 2008, Beuth Verlag GmbH: Berlin
29. DIN EN ISO 148–1:2017–05, in Metallic materials – Charpy pendulum impact test – Part 1: Test method (ISO 148–1:2016). 2017, Beuth Verlag GmbH: Berlin
30. Andersson JO, Helander T, Hoglund LH, Shi PF, Sundman B (2002) THERMO-CALC & DICTRA, computational tools for materials science. *Calphad-Comput Coupling Phase Diagrams Thermochem* 26(2):273–312. [https://doi.org/10.1016/S0364-5916\(02\)00037-8](https://doi.org/10.1016/S0364-5916(02)00037-8)
31. Krauss G (1989) *Steels: Heat Treatment and Processing Principles*, ASM International
32. Liu T, Long M-J, Chen D-F, Duan H-M, Gui L-T, Yu S, Cao J-S, Chen H-B, Fan H-L (2018) Effect of coarse TiN inclusions and microstructure on impact toughness fluctuation in Ti microalloyed steel. *J Iron Steel Res Int* 25(10):1043–1053. <https://doi.org/10.1007/s42243-018-0149-5>
33. Vander Voort GF (2004) 9. *Metallography and microstructures*, ASM International
34. Schaupt T, Schroeder N, Schroepfer D, Kannengiesser T (2021) Hydrogen-assisted cracking in GMA welding of high-strength structural steel—a new look into this issue at narrow groove. *Met* 11(6):904
35. Jorge JCF, Souza LFGD, Mendes MC, Bott IS, Araújo LS, Santos VRD, Rebello JMA, Evans GM (2021) Microstructure characterization and its relationship with impact toughness of C-Mn and high strength low alloy steel weld metals – a review. *J Mater Res Technol* 10:471–501. <https://doi.org/10.1016/j.jmrt.2020.12.006>
36. Li Y, Feng Q, Cui S, Dai L, Liu Q, Jia S, Zhang H, Wu H (2024) Effect of Mo microalloying on impact toughness of X80 pipeline steel in SCGHAZ. *J Mater Res Technol* 28:2648–2659. <https://doi.org/10.1016/j.jmrt.2023.12.117>
37. Mohrbacher H (2010) Principal effects of Mo in HSLA steels and cross effects with microalloying elements. *Cent Iron Steel Res Inst*. pp 75–96
38. Saha DC, Nayak SS, Biro E, Gerlich AP, Zhou Y (2014) Mechanism of secondary hardening in rapid tempering of dual-phase steel. *Metall Mater Trans A* 45:6153–6162. <https://doi.org/10.1007/s11661-014-2591-8>
39. Danoix F, Danoix R, Akre J, Grellier A, Delagnes D (2011) Atom probe tomography investigation of assisted precipitation of secondary hardening carbides in a medium carbon

- martensitic steels. *J Microsc* 244(3):305–310. <https://doi.org/10.1111/j.1365-2818.2011.03537.x>
40. Cizek P, Wynne B, Davies CHJ, Hodgson PD (2015) The effect of simulated thermomechanical processing on the transformation behavior and microstructure of a low-carbon Mo-Nb line-pipe steel. *Metall Mater Trans A* 46:407–425. <https://doi.org/10.1007/s11661-014-2601-x>
41. Mohrbacher H (2018) Property optimization in as-quenched martensitic steel by molybdenum and niobium alloying. *Met* 8. <https://doi.org/10.3390/met8040234>
42. Powell GLF, Herfurth G (1998) Charpy V-notch properties and microstructures of narrow gap ferritic welds of a quenched and tempered steel plate. *Metall Mater Trans A* 29(11):2775–2784. <https://doi.org/10.1007/s11661-998-0318-4>
43. Lee J-L (1994) Evaluation of the nucleation potential of intragranular acicular ferrite in steel weldments. *Acta Metall Mater* 42(10):3291–3298. [https://doi.org/10.1016/0956-7151\(94\)90461-8](https://doi.org/10.1016/0956-7151(94)90461-8)

Publisher's Note Springer Nature remains neutral with regard to jurisdictional claims in published maps and institutional affiliations.